# Geochemical and H–O–Sr–B isotope signatures of Yangyi geothermal fields: implications for the evolution of thermal fluids in fracture-controlled type geothermal system, Tibet, China

Rui Cao[1,2], Ji Dor[1,2,3*], YongQiang Cai[1], XiaoLin Chen[4], Xiang Mao[5] and Hui-ren Meng[1]

*Correspondence:
cdut_dorji@163.com

[1] State Key Laboratory
of Geohazard Prevention
and Geoenvironment
Protection, Chengdu University
of Technology, Chengdu 610059,
China
[2] College of Engineering, Tibet
University, Lhasa 850000, China
[3] Chinese Academy
of Engineering, Beijing 100088,
China
[4] Dangxiong County Yangyi
Geothermal Power Plant Co., Ltd.,
Tibet 851500, China
[5] New Energy Research Institute,
SINOPEC Star Petroleum Co., Ltd,
Beijing 100083, China

## Abstract

High-temperature hydrothermal systems are mainly distributed in the north–south graben systems of southern Tibet as an important part of the Mediterranean–Tethys Himalayan geothermal belt in mainland China. As the largest unit capacity and second stable operating geothermal power station in China, Yangyi is the fracture-controlled type geothermal field in the center of Yadong–Gulu Graben. In this paper, hydrogeological and hydrochemical characteristics, isotope composition ($\delta D$ and $\delta^{18}O$, $^{87}Sr/^{86}Sr$ and $\delta^{11}B$) of borehole water, hot springs, and surface river samples were analyzed. From the conservative elements (such as $Cl^-$ and $Li^+$) and $\delta D$ and $\delta^{18}O$ values, the geothermal water of the Yangyi high-temperature geothermal field is estimated to be of meteoric origin with the contributions of chemical components of the magmatic fluid, which is provided by partially molten granite as a shallow magmatic heat source. According to logging data, the geothermal gradient and terrestrial heat flow value of the Yangyi high-temperature geothermal field are 6.48 ℃/100 m and 158.37 mW m$^{-2}$, respectively. Combining the hydrothermal tracer experiment, $^{87}Sr/^{86}Sr$ and $\delta^{11}B$ ratios obtained with gradually decreasing reservoir temperatures from the Bujiemu stream geothermal zone to Qialagai stream geothermal zone, we suggested the deep geothermal waters were mixed with local cold groundwater and then flow northeastward, forming the shallow reservoir within the crushed zone and intersect spot of faults in the Himalayan granitoid. Furthermore, in the process of ascent, the geothermal water is enriched in $K^+$, $Na^+$, and $HCO_3^-$ during the interaction with underlying Himalayan granitoid and pyroclastic rocks that occur as wall rocks. The detailed description and extensive discussion are of great significance for the further exploitation and utilization of north–south trending geothermal belts in Tibet.

**Keywords:** Yangyi geothermal fields, Water–rock reaction, Evolution of thermal fluids, Tibet

## Introduction

In recent years, with the increasing demand for global energy, declining of conventional energy reserves, and global climate change, the development and utilization of renewable energy has become an important energy development strategy for all countries around the world. (Michael et al. 2010; Karlsdottir et al. 2020). As an important renewable energy resource, geothermal resources have a broad prospect of development and utilization, and they are untouched by weather variations as the season progresses (Dincer and Acar 2015).

High-temperature hydrothermal systems are mainly distributed in the north–south graben systems of southern Tibet as an important part of the Mediterranean–Tethys Himalayan geothermal belt in mainland China (Dor et al. 2017). As the first geothermal power station in China to recharge geothermal fluids completely, Yangyi is the second steady operation of electric power with the largest unit capacity in China.

Recently, more than 60 natural springs have been found in the Yangyi high-temperature geothermal field (YHGF). Most of these springs have temperatures of > 80℃, and more than half of springs' temperatures exceed the local water boiling point. After the geothermal geological survey and geophysical exploration, more than 30 boreholes have been drilled. Well No. 203, No. 200, No. 208, and No. 403 have a power generation of up to 30 MW with the measured temperature range from 104 to 207 ℃. Among them, well No. 208 and No. 203 were already used as production wells. Especially as the main production well, well No. 208 had a total production of geothermal water and steam up to 402.8 t/h with the highest measured temperature near 207 ℃ and an electricity generation potential of 10 MW (Jin and Cheng 1992; Zhang et al. 1993). However, few research developments have been discussed in recent 10 years. Previous studies of the YHGF have focused on the hydrothermal alteration (Qin 2003), Hydrogeochemistry and environmental impact of geothermal waters (Guo et al. 2009), investigation of the deep structures using converted waves (Zhang et al. 1993), and application of synthetic geophysical exploration methods (Jin and Cheng 1992). Furthermore, few studies have focused on the heat transfer model, evolution of thermal fluids, and recharge, runoff, and discharge conditions in the YHGF. Moreover, the detailed description and extensive discussion are expected to be valuable materials for the further exploitation and utilization of the geothermal field.

In this article, the new hydrochemical, oxygen, and hydrogen isotopic data of hot springs and borehole water samples were used to determine the origin of geothermal fluids and calculate the reservoir temperature. In combination with the boron and strontium isotopic characteristics of geothermal fluids, which have not been studied in the study area before, we have gained a better understanding of water–rock interaction and mixing evaluation of deep geothermal fluid with cold groundwater. In addition, by combining the hydrothermal tracer experiment, characteristics of the main fractures of heat conduits, and geophysical and drilling exploration in the YHGF, we discussed the evolution of the geothermal fluid and created a new conceptual model for the fracture-controlled type geothermal field in the north–south graben systems of southern Tibet.

## Geological setting and geothermal activities

The terranes of the Tibetan Plateau are composed of a series of east–west trending blocks: Songpan–Ganzi, Qiantang, Lhaza, and the Himalayas (Wang et al. 2015; Yin 2000). These four sub-blocks are separated by the Jinshajiang Suture Zone, Bangong–Nujiang Suture Zone, and the Indus–Yarlung Zangbo Suture Zone (Hou et al. 2004). Due to the east–west extension of the Tibetan Plateau, a series of extensional structures have developed in Southern Tibet of the Tibetan Plateau, resulting in the formation of six north–south grabens (Armijo et al. 1986; Ha 2019). The hot springs in southern Tibet are mainly distributed along the north–south graben, which can be divided into six nearly north–south trending geothermal belts (Fig. 1a): Riduo–Cuona geothermal zone, Yadong–Gulu geothermal zone, Shenza–Dingjie geothermal zone, Danggyongcuo–Taggai geothermal zone, Cangmucuo–Palongcuo geothermal zone, and Yare–Gongzhucuo geothermal zone.

The YHGF is located in the center of Yadong–Gulu graben, which is the most developed and longest graben system in the Qinghai–Tibet Plateau, with a length of ~500 km (Wang et al. 2018a, b). It belongs to Yadong–Gulu geothermal zone, with altitude varying from 4550 to 5050 m. The basement of the YHGF is composed of Early Himalayan porphyry granite and granite porphyry that are covered by Miocene volcanic rocks (trachyandesite, trachyte, tuff, and volcanic breccia) and Pliocene
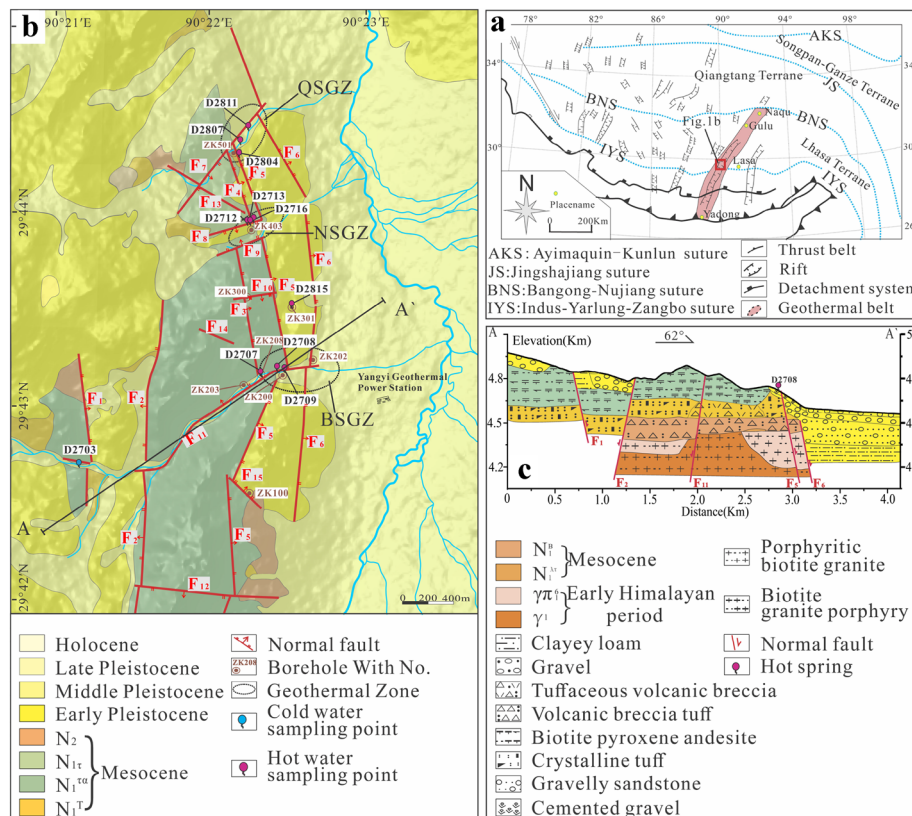


**Fig. 1** **a** Geological sketch of main geothermal belts in Tibet (modified from Wang et al. 2020); **b** simplified geological map of YHGF (modified from The Geothermal Geological Team of Tibet 1990); **c** geological cross sections between A and A′

sediments (Fig. 1b, c). The major structures of the YHGF can be divided into three groups: (1) the near north–south stretching fault, with the striking angles ranging from 313° to 23°, are the main tectonic crack of heat controller for the hydrothermal activity in YHGF (Fig. 2a, b), including $F_1$, $F_2$, $F_3$, $F_4$, $F_5$, and $F_6$. Except for $F_1$ (51°–58°), the dip angle of all the other faults generally exceeds 70°; (2) the near east–west stretching fault, with strike varying from 30° to 95° and dip angle generally exceeds 60°, including $F_7$, $F_8$, $F_9$, $F_{10}$, $F_{11}$, and $F_{12}$, except for $F_6$ is a hidden fault, all the other faults developed in the study area have obvious surface manifestation, such as scratches, steps and fault fracture zone (Fig. 2c); and (3) the northwest–southeast stretching fault, including $F_{13}$, $F_{14}$, $F_{15}$. The geothermal activity of the YHGF is exposed in the junction of near-east–west and near-north–south faults (Fig. 2d).

The hydrothermal activities of YHGF are mainly distributed in the piedmont of the west of the Yangyi sub-basin. The hydrothermal activities are clearly zoned in the YHGF and are subdivided into Bujiemu, Nangzeng, and Qialagai stream geothermal zone from south to north, as described in detail below.
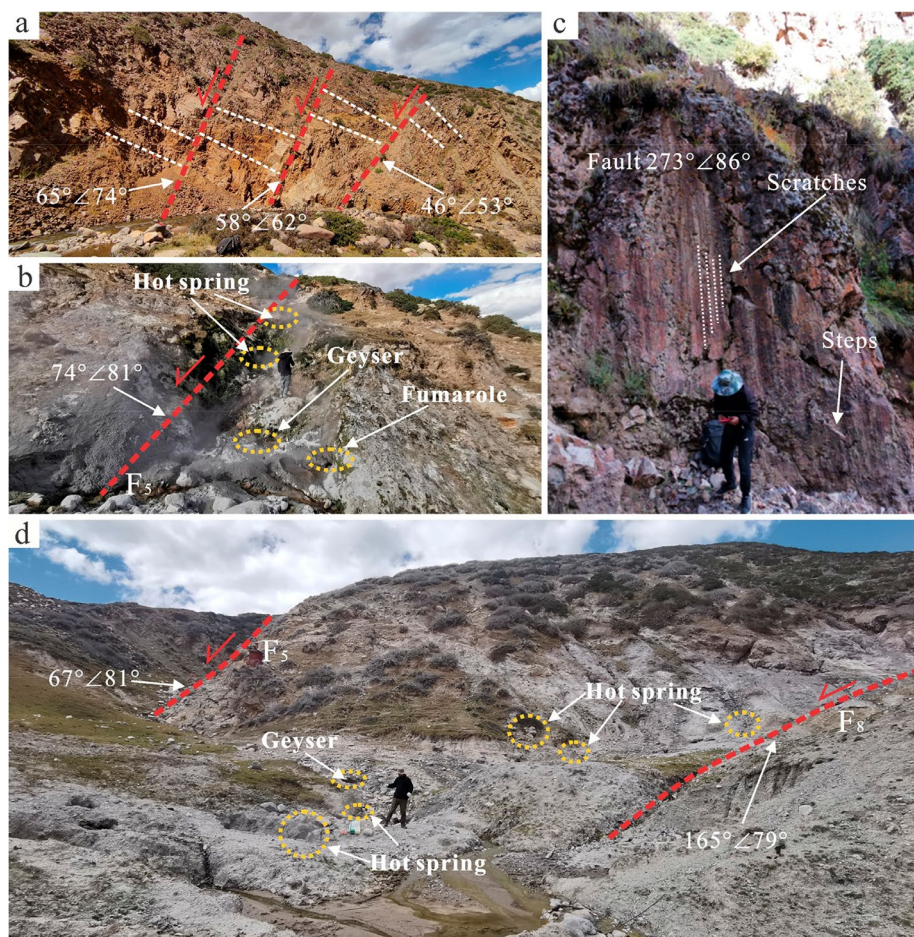


**Fig. 2** Extensional structures in the YHGF. **a** Three secondary faults near $F_{11}$; **b** hot springs, Geyser and fumarole are distributed along $F_5$; **c** scratches and steps of $F_7$; **d** geothermal activity is exposed in the junction of $F_8$ and $F_5$

The Bujiemu Stream geothermal zone (BSGZ) is located at the junction of $F_3$, $F_5$, and $F_{11}$ at the mountain pass of the Bujiemu Stream (Fig. 1b). The geothermal manifestations of BSGZ are dominated by high-temperature springs ($\geq 80$ ℃) and travertine sedimentation. The discharges of high-temperature springs are between 0.001 and 0.5 L/s. Seven drilling wells (ZK202, ZK203, ZK204, ZK206, ZK208, ZK211, and ZK212) are distributed in BSGZ, of which ZK208 and ZK203 are the production wells at present.

The Nangzeng Stream geothermal zone (NSGZ) is located at the junction of $F_4$, $F_5$, $F_8$, and $F_9$ in the valley of the Nangzeng Stream. The geothermal manifestations of NSGZ are dominated by hot spring group, fumarole, and hydrothermal alteration (Fig. 1b). Six hot springs occur on NSGZ and have a temperature and discharge range from 74.5 to 86.1 ℃ and 0.001 to 0.05L/s, respectively. The hot waters discharge from the hot spring and flow into the Nangzeng Stream. The main types of hydrothermal alteration in NSGZ are smectitization, kaolinization, and aluminization (Qin 2003; Tan 1992). Four drilling wells (ZK400, ZK401, ZK402, and ZK403) are distributed along the Nangzeng stream, of which ZK403 is the major recharge well at present.

The Qialagai Stream geothermal zone (QSGZ) is located at the junction of $F_4$, $F_5$, and $F_7$ at the Qialagai Stream. The geothermal manifestations are dominated by hot springs and hydrothermal alteration (smectitization and geyserite). More than 50 hot springs are exposed in this area, and most of them are high-temperature springs ($T > 60$ ℃), with a discharge between 0.001 and 0.5 L/s. The hot waters discharge from the hot spring and flow into the Qialagai Stream. Five drilling wells (ZK500, ZK501, ZK502, ZK503, and ZK505) are distributed along the Qialagai stream.

## Samples and analytical procedure

Eleven water samples were collected in September–October 2021 from the YHGF: four borehole water samples (D2707, D2709, D2807, and D2815), Six from hot springs (D2708, D2712, D2713, D2716, D2804, and D2807), and one surface water sample (D2703). As shown in Fig. 1b, two water samples from borehole water (D2707 and D2709) and one from hot springs (D2708) were collected in the BSGZ, three water samples from hot spring in NSGZ (D2712, D2713, and D2716) and one from borehole water (D2811), and two water samples from hot spring (D2804 and D2807) in QSGZ. One surface river sample (D2703) was collected from the Qialagai Stream, and one from borehole ZK301 (D2815) between the BSGZ and NSGZ.

All samples were filtered through 0.45 µm membranes on site. The sampling locations are shown in Fig. 1b. Except for the D2709 was collected in the recharge water of ZK208 at Yangyi geothermal power station, all the other borehole hot waters were collected in the unclosed borehole. All water samples were stored in 500 and 1500 mL polyethylene bottles. For each sampling site, three different types of samples were collected: (1) a 1500 mL liquid sample for major anions measurements; (2) a 500 mL liquid sample acidified by $HNO_3$ for cations analysis; (3) a 500 mL liquid sample for H–O isotope, $^{87}Sr/^{86}Sr$ and $\delta^{11}B$ analysis. In-situ field measurements of temperature, electrical conductivity (EC), total dissolved solids (TDS), and PH of water samples were performed using pH/EC/TDS tester (HANNA HI98129; accuracy: $\pm 0.05, \pm 2\%, \pm 2\%$) and probe-type thermometer (accuracy: $\pm 0.1$ ℃). The results of sampling and measurement are listed in Table 1.

Cao *et al. Geothermal Energy* (2023) 11:23

Page 6 of 28

**Table 1** Chemical composition and physicochemical parameters of water samples in YHGF

| Location | Sample No | Sample type | T (°C) | pH | TDS (mg/L) | Ca (mg/L) | Mg (mg/L) | Na (mg/L) | K (mg/L) | Cl (mg/L) | HCO$_3$ (mg/L) | CO$_3$ (mg/L) | SO$_4$ (mg/L) | Si (mg/L) | SiO$_2$ (mg/L) | Sr (mg/L) | B (mg/L) | Li (mg/L) | F (mg/L) | Hadrochemical type |
|---|---|---|---|---|---|---|---|---|---|---|---|---|---|---|---|---|---|---|---|---|
| BSGZ | D2707 | Borehole water | 88.7 | 9.1 | 1454 | 3.8 | 0.1 | 360 | 33 | 152 | 390 | 54 | 203 | 62 | n.a | 0.25 | 27.95 | 13.31 | 21.11 | Na–Cl |
| | D2708 | Hot spring | 85.4 | 8.0 | 817 | 33.5 | 9.6 | 179 | 13 | 84 | 422 | n.d | 86 | 82 | n.a | 0.98 | 12.65 | 4.88 | 2.12 | Na–HCO$_3$–Cl |
| | D2709 | Borehole water | 46.0 | 7.0 | 1517 | 9.8 | 0.2 | 399 | 37 | 152 | 606 | n.d | 203 | 65 | n.a | 0.52 | 29.27 | 10.71 | 14.66 | Na–HCO$_3$ |
| | YYT-6* | Borehole water | 89.0 | 8.0 | 1799 | 6.5 | 1.0 | 490 | 57 | 183 | 645 | 29 | 256 | n.a | 377 | 0.47 | 45.50 | 10.50 | 20.50 | Na–HCO$_3$ |
| | YYT-7* | Borehole water | 84.0 | 7.9 | 1733 | 6.6 | 0.9 | 479 | 51 | 180 | 639 | 24 | 247 | n.a | 350 | 0.43 | 44.00 | 9.51 | 20.00 | Na–HCO$_3$ |
| | YYT-8* | Borehole water | 86.0 | 8.0 | 1827 | 25.8 | 1.0 | 597 | 41 | 185 | 815 | 51 | 255 | n.a | 195 | 0.83 | 45.70 | 6.64 | 13.00 | Na–HCO$_3$ |
| | ZK204^ | Borehole water | 82.0 | 8.4 | 1782 | 15.8 | 0.8 | 562 | 32 | 184 | 840 | n.d | 240 | n.a | 209 | n.a | 29.99 | 6.42 | 13.68 | Na–HCO$_3$ |
| | CHK4^ | Borehole water | 46.0 | 7.8 | 907 | 37.5 | 11.4 | 210 | 17 | 82 | 504 | n.d | 125 | n.a | 174 | n.a | 14.93 | 5.31 | 5.13 | Na–HCO$_3$–Cl |
| | ZK207^ | Borehole water | 83.0 | 8.1 | 1568 | 13.0 | 2.6 | 464 | 34 | 172 | 820 | n.a | 188 | n.a | 231 | n.a | 29.75 | 12.24 | 11.51 | Na–HCO$_3$ |
| NSGZ | D2712 | Hot spring | 85.0 | 7.8 | 1244 | 16.0 | 0.7 | 364 | 20 | 150 | 529 | n.d | 200 | 46 | n.a | 0.41 | 27.55 | 12.52 | 11.93 | Na–HCO$_3$–Cl |
| | D2713 | Hot spring | 79.8 | 9.3 | 1264 | 3.1 | 0.6 | 326 | 24 | 149 | 258 | 66 | 209 | 67 | n.a | 0.33 | 27.76 | 12.28 | 19.23 | Na–Cl |

Cao et al. Geothermal Energy    (2023) 11:23

Page 7 of 28

**Table 1** (continued)

| Location | Sample No | Sample type | T (°C) | pH | TDS (mg/L) | Ca (mg/L) | Mg (mg/L) | Na (mg/L) | K (mg/L) | Cl (mg/L) | HCO₃ (mg/L) | CO₃ (mg/L) | SO₄ (mg/L) | Si (mg/L) | SiO₂ (mg/L) | Sr (mg/L) | B (mg/L) | Li (mg/L) | F (mg/L) | Hadrochemical type |
|---|---|---|---|---|---|---|---|---|---|---|---|---|---|---|---|---|---|---|---|---|
| | D2716 | Hot spring | 86.1 | 9.2 | 1249 | 3.3 | 0.1 | 323 | 19 | 147 | 282 | 54 | 205 | 64 | n.a | 0.34 | 27.75 | 12.33 | 18.98 | Na–Cl |
| | D2815 | Bore-hole water | 74.5 | 8.4 | 1612 | 9.0 | 0.1 | 416 | 33 | 172 | 574 | n.d | 231 | 54 | n.a | 0.41 | 31.67 | 11.44 | 16.41 | Na–Cl |
| | ZK401^ | Bore-hole water | 84.0 | 8.6 | 1516 | 11.1 | 1.7 | 458 | 31 | 171 | 631 | n.a | 235 | n.a | 193 | n.a | 28.89 | 7.82 | 11.52 | Na–HCO₃–Cl |
| QSGZ | D2804 | Hot spring | 85.8 | 8.5 | 1115 | 2.2 | 0.1 | 292 | 16 | 143 | 262 | 21 | 191 | 72 | n.a | 0.15 | 24.15 | 9.74 | 18.85 | Na–Cl |
| | D2807 | Hot spring | 84.6 | 9.6 | 1431 | 2.0 | 0.1 | 375 | 21 | 171 | 242 | 102 | 232 | 62 | n.a | 0.31 | 30.44 | 13.01 | 24.65 | Na–Cl |
| | D2811 | Bore-hole water | 46.3 | 9.2 | 1214 | 6.8 | 0.2 | 316 | 17 | 147 | 271 | 61 | 197 | 64 | n.a | 0.50 | 23.45 | 10.38 | 19.49 | Na–Cl |
| | YYT-1* | Hot spring | 84.0 | 9.2 | 1277 | 3.8 | 1.0 | 374 | 24 | 169 | 179 | 100 | 225 | n.a | 218 | 0.33 | 40.80 | 7.78 | 20.40 | Na–Cl |
| | YYT-2* | Hot spring | 79.0 | 9.2 | 1398 | 1.4 | 0.9 | 430 | 25 | 175 | 223 | 119 | 245 | n.a | 216 | 0.27 | 42.40 | 8.41 | 21.60 | Na–Cl |
| | YYT-3* | Hot spring | 86.0 | 9.4 | 1431 | 1.1 | 1.1 | 433 | 29 | 182 | 148 | 152 | 253 | n.a | 226 | 0.23 | 44.60 | 9.11 | 22.70 | Na–Cl |
| | YYT-4* | Hot spring | 88.0 | 9.1 | 1416 | 1.5 | 1.0 | 440 | 25 | 174 | 242 | 127 | 242 | n.a | 212 | 0.16 | 41.40 | 8.50 | 22.30 | Na–Cl |
| | Q502^ | Hot spring | 50.0 | 8.5 | 1196 | 4.8 | 0.0 | 363 | 12 | 152 | 395 | n.a | 84 | n.a | 147 | n.a | 25.85 | 11.52 | 24.70 | Na–HCO₃–Cl |
| | Q572^ | Hot spring | 50.0 | 7.6 | 624 | 16.4 | 0.3 | 180 | 8 | 83 | 370 | n.a | 44 | n.a | 80 | n.a | 14.43 | 5.01 | 8.36 | Na–HCO₃ |
| | D2703 | Surface water | 9.0 | 7.4 | 66 | 8.1 | 1.6 | 3.2 | 0.7 | 6.9 | 24.8 | n.d | 5.9 | 7.5 | n.a | 0.07 | 0.96 | 0.01 | 0.33 | Ca-Mg-HCO₃ |

Cao *et al. Geothermal Energy* (2023) 11:23

Page 8 of 28

**Table 1** (continued)

| Location | Sample No | Sample type | T (°C) | pH | TDS (mg/L) | Ca (mg/L) | Mg (mg/L) | Na (mg/L) | K (mg/L) | Cl (mg/L) | HCO₃ (mg/L) | CO₃ (mg/L) | SO₄ (mg/L) | Si (mg/L) | SiO₂ (mg/L) | Sr (mg/L) | B (mg/L) | Li (mg/L) | F (mg/L) | Hadrochemical type |
|---|---|---|---|---|---|---|---|---|---|---|---|---|---|---|---|---|---|---|---|---|
| | YYC-2* | Surface water | 13.3 | 7.1 | 60 | 12.5 | 1.6 | 4.0 | 0.4 | 1.8 | 51.3 | n.d | 3.1 | n.a | 10.1 | 0.07 | 0.57 | 0.00 | 0.19 | Ca-Mg-HCO₃ |
| | YYC-3* | Surface water | 13.6 | 7.2 | 64 | 11.8 | 1.8 | 4.8 | 0.5 | 2.3 | 45.8 | n.d | 7.3 | n.a | 11.5 | 0.08 | 0.65 | 0.02 | 0.25 | Ca-Mg-HCO₃ |
| | YYC-4* | Surface water | 13.8 | 7.9 | 70 | 12.8 | 2.3 | 5.5 | 0.5 | 2.7 | 46.6 | 0.2 | 8.9 | n.a | 12.5 | 0.10 | 0.67 | 0.03 | 0.31 | Ca-Mg-HCO₃ |
| | YYC-1* | Surface water | 16.0 | 7.6 | 80 | 15.6 | 2.5 | 5.0 | 0.5 | 1.9 | 60.3 | 0.2 | 5.0 | n.a | 18.4 | 0.12 | 0.72 | 0.01 | 0.32 | Ca-Mg-HCO₃ |

"*" means the data obtained from Yuan et al. (2014); "^" means the data obtained from The Geothermal Geological Team of Tibet (1990); n.a. = not analyzed; n.d.: not detected

Major chemical components of water samples were determined at the Key Laboratory of Geothermal Resources Development and Utilization, Sinopec. Concentrations of major cations ($Na^+$, $K^+$, $Ca^{2+}$, $Mg^{2+}$, $B^{3+}$, $Si^{4+}$, $Sr^{2+}$ and $Li^+$) and major anions ($F^-$, $Cl^-$, $HCO_3^-$ and $SO_4^{2-}$) were determined by ion chromatography (Dionex ICS-1100) with uncertainties of less than 2%. Calculated charge balance errors for most samples were within 5%, and all the samples were within 10%.

The values of stable oxygen and hydrogen isotope of water samples were analyzed by Mat-253 gas isotope mass spectrometer at The Analysis and testing research center of Beijing Research Institute of Uranium Geology. The $CO_2$ equilibration method was employed to measure the $^{18}O/^{16}O$ ratio; for the D/H ratio, the $H_2$ was generated by the Zn-reduction method (Coleman et al. 1982). Isotope ratios of $CO_2$ and $H_2$ were measured using a MAT-251 mass spectrometer, and the fractionation factor between $CO_2$ and water at 25 ℃ was assumed to be 1.0412 (Coplen 1988). The δD and $δ^{18}O$ values were referred to Vienna Standard Mean Ocean Water (V-SMOW), where $δ = (Rsample/Rstandard - 1) \times 1000$‰.

The values of $^{87}Sr/^{86}Sr$ and $δ^{11}B$ were determined by a Phoenix hot surface ionization mass spectrometer at The Analysis and testing research center of the Beijing Research Institute of Uranium Geology. 40 mL of sample was heated in a Teflon vessel to determine $^{87}Sr/^{86}Sr$ ratios. The residue was then dissolved in distilled HCl and centrifuged to remove any precipitate. Sr was separated from other ions by eluting an aliquot through a quartz cation exchange column packed with Eichrom Sr-Spec resin. The $^{87}Sr/^{86}Sr$ ratio measurement error is 2σ and applies to the last decimal place. The B isotopic value in this study is expressed in δ, and the reproducibility is 2σ for $δ^{11}B$. The parallel sample used for the test is D2811, the relative error of parallel samples is below 15%.

## Results

### Hydrochemical characteristics

The chemical composition of the studied waters and physicochemical parameters such as temperature, pH, and total dissolved solids (TDS) are listed in Table 1. The measured temperatures of the borehole waters and hot springs in the YHGF range from 46–89℃ to 50–88 ℃, respectively. Most hot springs and borehole water temperatures were around 85 ℃, indicating their temperatures were near or even above the boiling points already. The hot springs and borehole water are near neutral to alkaline in nature, with pH varying from 7.0 to 9.6. TDS of the hot springs and borehole water are in the range of 624–1431 mg/L and 907–1827 mg/L, respectively. The surface river water had lower temperatures (9–16 ℃), and TDS (60–80 mg/L), with pH values over 7.

The silica concentrations of the surface cold water varied from 5 mg/L to 9 mg/L. A higher concentration of dissolved silica is found in the hot springs and borehole thermal waters, with silica concentrations ranging from 37 mg/L to 176 mg/L, particularly those usually associated with high-temperature magma geothermal systems (Giggenbach et al. 1983).

The concentrations of the cations ($Na^+$, $K^+$, $Ca^{2+}$, and $Mg^{2+}$) and anions ($HCO_3^-$, $Cl^-$ and $SO_4^{2-}$) in the water samples are plotted in the Piper diagram (Fig. 3). The borehole waters and hot springs, mostly plot along $Na–HCO_3$ and Na–Cl facies, contained $Na^+$ and $K^+$ as the predominant cation and either $HCO_3^-$ of $Cl^-$ as the predominant anion.
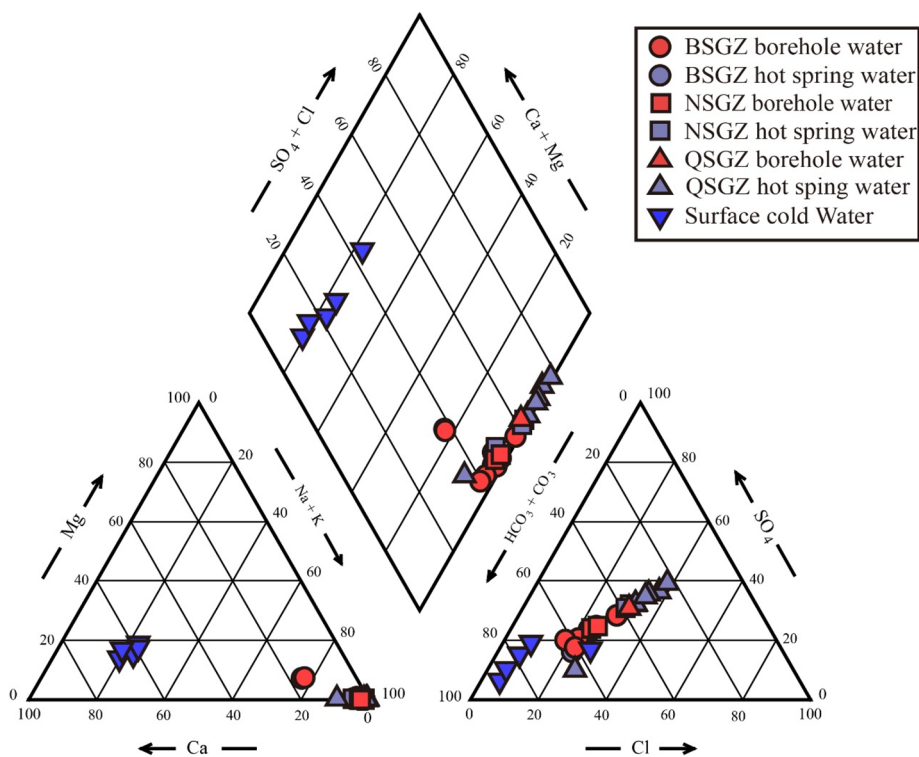
**Fig. 3** Pieper diagram for water samples from YHGF

In contrast to the thermal water, the surface cold water plot along $Ca–Mg–HCO_3$ facies with $Ca^{2+}$ as the predominant cation and either $HCO_3^-$ as the predominant anion. The thermal water in BSGZ fall in $Na–HCO_3$ or $Na–HCO_3–Cl$ type facies, NSGZ fall in $Na–HCO_3–Cl$ or $Na–Cl$ facies, and QSGZ fall in $Na–Cl$ facies, respectively. Therefore, chloride is the dominant anion in geothermal waters, while that in surface cold water is bicarbonate.

The geochemistry of trace elements, such as Sr, B, Li, and F, are listed in Table 1. The surface cold water contained only low concentrations of the trace elements, with the concentrations of Sr, B, Li, and F ranging from 0.07 to 0.12 mg/L (average 0.09 mg/L), 0.57–0.96 mg/L (average 0.71 mg/L), 0–0.03 mg/L (average 0.01 mg/L) and 0.19–0.33 mg/L (average 0.28 mg/L), respectively. However, a significant difference was observed in the trace element concentration between the geothermal waters and surface cold water. The concentrations of Sr, B, Li, and F in the hot springs and borehole thermal waters ranged from 0.15 to 0.98 mg/L (average 0.41 mg/L), 12.65–45.7 mg/L (average 30.91 mg/L), 4.88–13.31 mg/L (average 9.54 mg/L) and 2.12–24.7 mg/L (average 16.64 mg/L), respectively.

### Oxygen and hydrogen isotopic characteristics of YHGF

The $\delta D$ and $\delta^{18}O$ isotopic composition of the samples from the YHGF vary range from $-164.8$ to $-132.9‰$ and from $-21.9$ to $-17.75‰$, respectively. As shown in Table 2, for the hot springs, the $\delta D$ and $\delta^{18}O$ values ranged from $-164.1$ to $-151‰$ and from $-21.2$ to $-17.75‰$, respectively. The borehole water has wider $\delta D$ and $\delta^{18}O$ values, varied

**Table 2** δD and δ$^{18}$O values, δ$^{11}$B isotopic ratio and $^{87}$Sr/$^{86}$Sr isotopic ratio of water samples collected in YHGF

| Location | Sample No | type | δD (‰) SMOW | δ$^{18}$O(‰) SMOW | δ$^{11}$B(‰) | $^{87}$Sr/$^{86}$Sr | Recharge elevation (m) |
|---|---|---|---|---|---|---|---|
| BSGZ | D2707 | Borehole water | − 164.8 | − 21.9 | − 2.33 | 0.7063 | 5647.5 |
| | D2708 | Hot spring | − 151 | − 19.8 | − 4.74 | 0.71094 | 5302.5 |
| | D2709 | Borehole water | n.a | n.a | − 3.44 | 0.70673 | – |
| | ZK204^ | Borehole water | − 132.9 | − 18.08 | n.a | n.a | 4580 |
| | CHK4^ | Borehole water | − 134.65 | − 19.5 | n.a | n.a | 4893.75 |
| | Q6^ | Hot spring | − 155.6 | − 18.82 | n.a | n.a | 5417.5 |
| | ZK200^ | Borehole water | − 161.25 | − 18.01 | n.a | n.a | 5558.75 |
| | YYT-7* | Borehole water | n.a | n.a | − 9.7 | n.a | – |
| | YYT-8* | Borehole water | n.a | n.a | − 6.7 | n.a | – |
| NSGZ | D2712 | Hot spring | − 160.7 | − 19.6 | − 3.09 | 0.70967 | 5545 |
| | D2716 | Hot spring | − 162.5 | − 21.2 | − 2.86 | 0.70983 | 5590 |
| | D2815 | Borehole water | n.a | n.a | − 4.18 | 0.70682 | – |
| | Q5^ | Hot spring | − 158.97 | − 18.55 | n.a | n.a | 5501.75 |
| | Q411^ | Hot spring | − 155 | − 18.43 | n.a | n.a | 5402.5 |
| | ZK401^ | Borehole water | − 163.8 | − 19.32 | n.a | n.a | 5622.5 |
| QSGZ | D2804 | Hot spring | − 164.1 | − 20.4 | − 3.72 | 0.7085 | 5630 |
| | D2811 | Borehole water | n.a | n.a | − 2.35 | 0.70886 | n.a |
| | ZK501 | Borehole water | − 160.8 | − 18.97 | n.a | n.a | 5547.5 |
| | Q7^ | Hot spring | − 155.9 | − 17.75 | n.a | n.a | 5425 |
| | Q4^ | Hot spring | − 158.8 | − 18.57 | n.a | n.a | 5497 |
| | YYT-1* | Hot spring | n.a | n.a | n.a | n.a | – |
| | YYT-4* | Hot spring | n.a | n.a | n.a | n.a | – |
| | YYC-2* | surface water | n.a | n.a | − 1 | n.a | – |
| | YYC-4* | surface water | n.a | n.a | − 3.9 | n.a | – |
| | YBJX1# | snow melting water | − 175 | − 24.5 | n.a | n.a | – |
| | YBJX2# | snow melting water | − 172 | − 24.2 | n.a | n.a | – |
| | ZK4001# | Deep geothermal water | − 139 | − 16 | n.a | n.a | – |
| | ZK329* | Borehole water | n.a | n.a | 12 | n.a | – |
| | ZK359* | Borehole water | n.a | n.a | 11.4 | n.a | – |
| | ZK357* | Borehole water | n.a | n.a | 123 | n.a | – |
| | ZK05* | Borehole water | n.a | n.a | 12 | n.a | – |
| | ZK4001* | Borehole water | n.a | n.a | 11.9 | n.a | – |
| | ZK302* | Borehole water | n.a | n.a | 11.6 | n.a | – |

"^" means the data obtained from The Geothermal Geological Team of Tibet (1990); "*" means the data obtained from Yuan et al. (2014); YBJX and ZK4001 was referred to Guo et al. (2010); n.a.: not analyzed

Cao *et al. Geothermal Energy*     (2023) 11:23

Page 12 of 28

from − 164.8 to − 132.9‰ and from − 21.9 to − 18.01‰, respectively. The hot springs were enriched in light oxygen compared to those of borehole water.

### B isotopic characteristics of the geothermal system

As the stable isotope, boron could be divided into $^{11}B$ and $^{10}B$, with a relative natural abundance of about 80.2% and 19.8% (Trupti et al. 2018). Due to the boron stable isotopic signature, the boron concentration and isotopic ratio were widely used to investigate the contamination and origin of boron dissolved in groundwaters (Pennisi et al. 2006; Musashi et al., 1988; Palmer and Sturchio 1990; Aggarwal et al. 2003), and analyze the geological genesis of geothermal systems (Mather and Porteous 2001) and geochemical evolution during the interaction between the host rocks and water (Dotsika et al. 2010; Yuan et al. 2014; Temizel et al., 2021). The boron isotopic analyses of the borehole water and hot spring samples from YHGF are listed in Table 2. The borehole water and hot spring samples have very narrow $\delta^{11}B$ values ranging from − 2.33 to − 9.7 ‰ and − 2.86 to − 4.74 ‰, respectively.
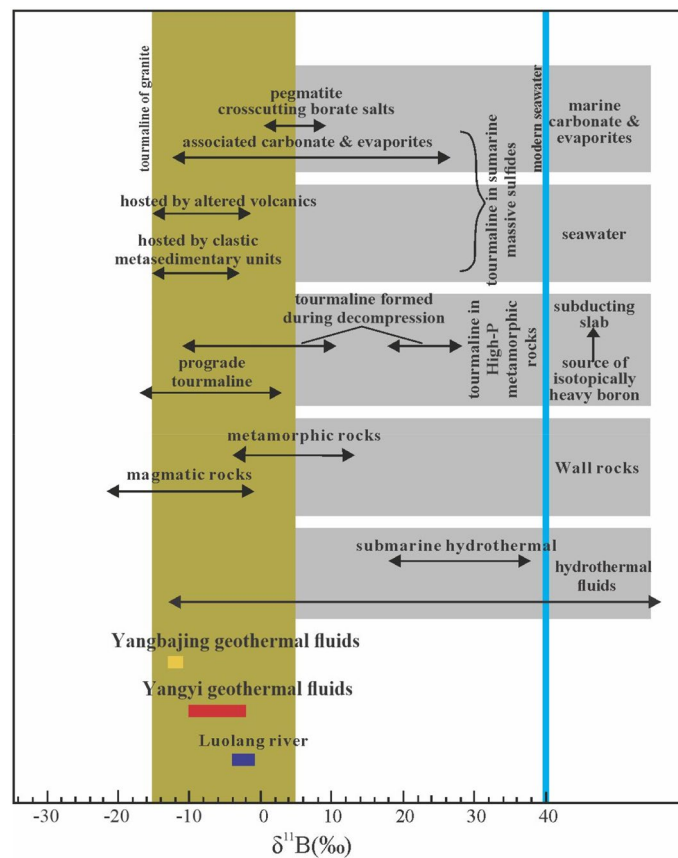


**Fig. 4** Simplified diagram of B isotope distribution in Yangzi and sambaing high-temperature geothermal field (modified from Cao et al 2021). The B isotopes of Yangban geothermal fluids from Yuan et al. (2014); The B isotope of hydrothermal fluids from Aggarwal et al. (2000), Palmer (1991) and Vengosh et al. (1991, 1994); Submarine hydrothermal was referred to Palmer and Slack (1989); The B isotope composition of granitic tourmalines was referred to Jiang et al. (1998); the B isotope composition of metamorphic rocks and magmatic rocks was referred to Zhou et al. (2019)

As Fig. 4 shown, the $\delta^{11}B$ values in the geothermal waters range from $-2.33‰$ to $-9.7‰$, similar to those of Luolang River waters ($-1.0‰$ to $-3.9‰$, Yuan et al. 2014) and hydrothermal fluids ($-10.5$ to $54.9‰$, Vengosh et al. 1994), suggesting the geothermal waters is typical hydrothermal fluids with the impact on groundwaters in YHGF, furthermore, due to the different PH dependent, Yangbajing geothermal waters are characterized by lower $\delta^{11}B$ values ($-11.4$ to $-12.8$ ‰) than those of Yangyi hot spring and borehole water samples (Dotsika et al. 2010).

### Sr isotopic characteristics of the geothermal system

The $^{87}Sr/^{86}Sr$ ratios varied from 0.7063 to 0.7109 for the borehole waters and hot springs samples, with an average value of 0.7085 (Table 2). The $^{87}Sr/^{86}Sr$ ratios of hot spring waters in Yangyi, Yangbajing, and Gudui geothermal field, Cretaceous strata of Tetori Group, and Cretaceous to Paleogene Kasagatake Rhyolites underlying the Hida Marginal Belt and the Hirayu Complex were plotted onto the $^{87}Sr/^{86}Sr$ ratio diagram. As Fig. 5 shown, the borehole waters and hot springs samples from YHGF are close to the reported $^{87}Sr/^{86}Sr$ ratios for the Himalayan granitoid and pyroclastic rocks. Furthermore, they have similar $^{87}Sr/^{86}Sr$ ratios to the geothermal water in Gudui geothermal field but lower $^{87}Sr/^{86}Sr$ ratios than the geothermal water in Yangbajing geothermal field.

## Discussion

### The origin of geothermal fluids in the YHGF

#### Recharge sources of YHGF

The linear relationship between $\delta^{18}O$ and $\delta D$ values of global meteoric water was first proposed by Craig (1961)

$$\delta D = 8\delta^{18}O + 10 \tag{1}$$
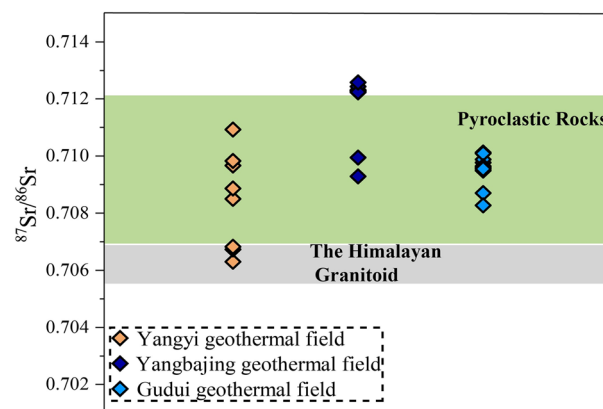


**Fig. 5** Sr isotope composition of YHGF, Yangbajing high-temperature geothermal field and Gudui high-temperature geothermal field. Data of Yangbajing high-temperature geothermal field are from Guo et al. (2010); Data of Gudui high-temperature geothermal field are from Wang et al. (2020). Data of Pyroclastic Rocks are from Jiang et al. (2018) and The Geothermal Geological Team of Tibet (1990); Data of The Himalayan Granitoid are from Shen et al. (2020)
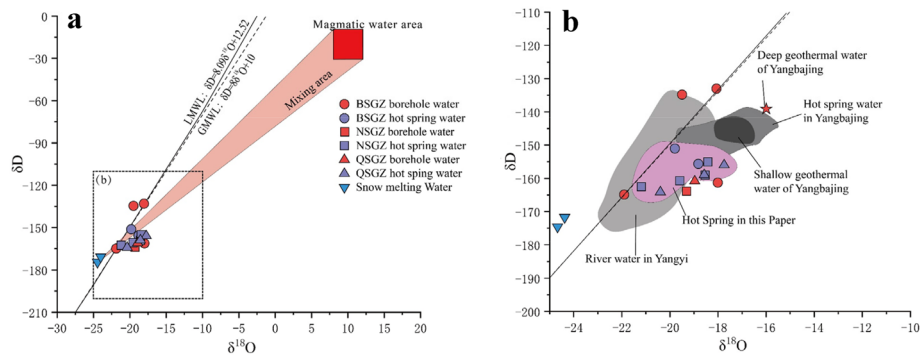
**Fig. 6 a** Plot of δD vs. $\delta^{18}$O for all water samples; GMWL and LMWL based on Craig (1961) and Wang (2017); the magmatic water area was referred to Giggenbach (1992); **b** comparison of hydrogen and oxygen isotope plots of geothermal water from Yangyi and Yangbajing (modified from Wang et al. 2020); River water in Yangyi was referred to The Geothermal Geological Team of Tibet (1990); Deep geothermal water and shallow geothermal water of Yangbajing was referred to Guo et al. (2010); Hot spring water of Yangbajing was referred to Zheng et al. (1982)

The southern Tibet meteoric line proposed by Wang (2017) is considered to be representative of the Local Meteoric Water Line with the following equation:

$$\delta D = 8.09\delta^{18}O + 12.52 \tag{2}$$

The measured $\delta^{18}$O and δD values from the investigated water samples are plotted and compared with the LMWL in Fig. 6. As shown in Fig. 6a, the hot spring, surface cold water plotted on or near the Local Meteoric Water Line, indicating that atmospheric precipitation is the main recharge source of geothermal water and surface streamflow in YHGF. Furthermore, most of the borehole waters and hot springs samples plot near the mixing region between meteoric and magmatic water, indicating the contribution of magmatic water to geothermal water (Fig. 6a, Pang 2006).

As conservative elements in geothermal water, the trace elements, such as $Cl^-$ and $Li^+$, are usually used to identify the source of the geothermal water (Bob et al. 2015). The average concentrations of Cl and Li in geothermal water are higher than that in surface cold water, indicating the contribution of other sources besides meteoric origin (Singh et al. 2014). The $\gamma Na^+/\gamma Cl^-$ ratios of geothermal water samples are much higher than one, and there were no salt-bearing strata in the YHGF, indicate abnormally high $Cl^-$ concentration was associated with the magmatic waters (Guo et al. 2012). Furthermore, the positive correlations between $Cl^-$ and $Li^+$, and $SO_4^{2-}$ also indicate that the magmatic materials, associated with the magmatic activity or degassing, are another resource of the geothermal water (Wang et al. 2017; Zhang et al. 2015).

In general, from the trace elements and δD and $\delta^{18}$O values, the geothermal water of the YHGF is estimated to be of meteoric origin and affected by a magmatic fluid contribution.

### Recharge elevation of YHGF

The $\delta^{18}$O and $\delta D$ values of atmospheric precipitation decrease with the increase of groundwater recharge elevation (Zheng 2000). Since many geothermal waters have evolved and exhibit $\delta^{18}$O drift, the $\delta D$ value is used in the calculation of recharge

elevation. Therefore, the recharge elevation of the geothermal fluid can be determined using the following equation:

$$H = (\delta D - \delta D_r)/k + h \tag{3}$$

where H is the elevation of recharge area (m); h is the elevation of sample point (m), the average value of the exposed elevation of the local hot spring 4700 m was adopted; $\delta D$ is the $\delta D$ value of the hot water (‰); $\delta D_r$ is the $\delta D$ value of the atmospheric precipitation, the data (− 126.9‰) collected by the local meteorological station was adopted(The Geothermal Geological Team of Tibet, 1990); and k is the negative gradient of δD with elevation (‰/100 m), the value (− 4‰/1000 m) proposed by Li and Pang (2022) was adopted. Therefore, the calculation equation of groundwater recharges elevation in this study is as follows:

$$H = [\delta D - (-126.9‰)]/(-4‰) * 1000 + 4700 \tag{4}$$

The calculation result of water samples determined by Eq. (4) is listed in Table 2. These results show that the recharge elevation of the geothermal water in BSGZ, NSGZ, and QSGZ range from 4850–5647.5 m, 5402.5–5622.5 m, and 5425–5630 m, respectively. Elevations above 5500 m on the Tibetan Plateau are covered with ice–snow accumulation all year round (Tan et al. 2014). Furthermore, the recharge elevation of the hot water of YHGF is close to the snow line. Therefore, the snow melt water infiltrates and supplies to the YHGF along faults. The terrain of the YHGF is generally high in the west and low in the east. The western mountain range is 5013 m–5884 m, and there is a height difference of 100–900 m compared with the geothermal field, indicating that gravitational potential energy is an important driving force for ice–snow melt water to supply geothermal fields.

### Reservoir temperature in the YHGF

#### *Chemical geothermometers*

The chemical geothermometers are established based on the equilibrium of water–gas–rock, which can be used to estimate the reservoir temperature in the geothermal system (Li et al. 2017a, b). Furthermore, the chemical geothermometers can be divided into the cation and silica geothermometers: (1) due to the exchange reaction of some cations (such as K–Mg, Na–K–Ca, and Na–K) in geothermal fluid rely on the temperature, the K–Mg, Na–K–Ca, and Na–K geothermometer are usually used as the cation geothermometer; (2) The $SiO_2$ concentration of hot water is stable, which is mainly determined by the solubility of silicon in water–rock interaction at a specific temperature. Therefore, the $SiO_2$ concentration can be used as an indicator of the reservoir temperature, such as quartz and chalcedony geothermometer.

The obvious limitation conditions were observed in the utilization of the cation geothermometer. The K–Mg geothermometer is suitable for the medium–low temperature geothermal field and is mainly used in estimating the temperature of shallower reservoirs. The Na–K geothermometers are adapted for high-temperature reservoirs (120–350 ℃) and are unsuitable for thermal water with pH < 7 and mixed water. The Na–K–Ca geothermometer is more suitable for geothermal water with high Ca contents (Zhu,
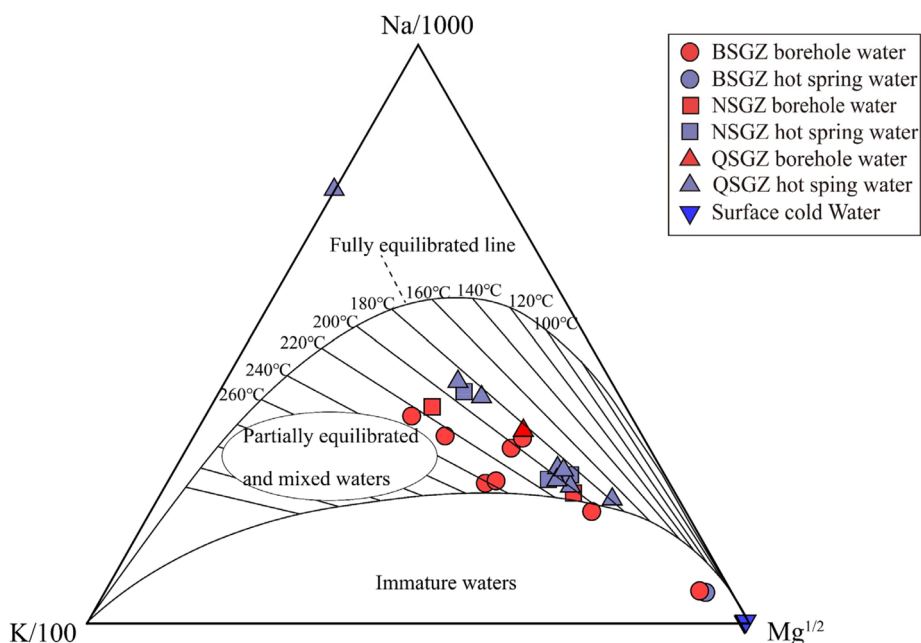
**Fig. 7** Na–K–Mg ternary diagram for the water samples in YHGF

1992). In particular, the YHGF belongs to the high-temperature geothermal system with low Ca contents (1.1 mg/L–37.5 mg/L) and has an obvious mixing process of deep geothermal fluid with cold groundwater. Furthermore, The Na–K–Mg triangle plot (Fig. 7) proposed by Giggenbach (1988) has been used to determine the equilibrium state. Figure 7 shows that except for the Q502 from QSGZ falls into the mature water area, and the CGK4, D0207, and D2708 from BSGZ fall into the immature water area, all the other samples fall into partially equilibrated and mixed water area, and away from the fully equilibrated line. Therefore, the cation geothermometer is not suitable for the YHGF.

The $SiO_2$ geothermometer is suitable for geothermal fields with reservoir temperatures ranging from 0 to 250 ℃ and is unsuitable for thermal water with pH < 7 and diluted hot water. In general, the $SiO_2$ geothermometer, such as quartz and chalcedony geothermometer, is mainly used to estimate reservoir temperature. The $SiO_2$ occurrence status of low-temperature thermal water in Iceland was reported by Arnórsson (1975). When the temperature < 110 ℃, the $SiO_2$ concentration is controlled by the solubility of chalcedony; in other cases, the $SiO_2$ concentration is controlled by the solubility of quartz. The reservoir temperatures of YHGF estimated by the quartz (maximum steam loss) geothermometer and quartz (no steam loss) geothermometer are listed in Table 3. The results obtained by the quartz (maximum steam loss) geothermometer are lower than those of the quartz (no steam loss) geothermometer and logging data. However, the results obtained by the quartz (no steam loss) geothermometer are close to the measurement result of the borehole. Furthermore, the quartz (no steam loss) geothermometer can provide more reliable results than the quartz (maximum steam loss) geothermometer. Therefore, the reservoir temperature of BSGZ, NSGZ, and QSGZ ranges from 153.31 to 227.72 ℃, 136.07 to 117.36 ℃, and 125.10 to 188.37 ℃, with an average reservoir temperature of 183.65, 154.75 and 166.71 ℃, respectively.

**Table 3** Calculation results of quartz geothermometer and silicon enthalpy mixture model

| Location | Sample No | Quartz [a] | Quartz [b] | Silica–enthalpy mixing model | |
|---|---|---|---|---|---|
| | | | | Temperature (℃) | Mixing proportion |
| BSGZ | D2707 | 153.31 | 146.20 | – | – |
| | D2708 | 171.41 | 161.15 | – | – |
| | D2709 | 156.89 | 149.17 | – | – |
| | YYT-6* | 227.72 | 206.46 | – | – |
| | YYT-7* | 221.50 | 201.54 | – | – |
| | YYT-8* | 178.27 | 166.77 | – | – |
| | ZK204^ | 183.12 | 170.72 | – | – |
| | CHK4^ | 170.66 | 160.54 | – | – |
| | ZK207^ | 189.99 | 176.30 | – | – |
| NSGZ | D2712 | 136.07 | 131.77 | 189.89 | 0.58445 |
| | D2713 | 158.63 | 150.61 | 251.8654 | 0.71929 |
| | D2716 | 156.01 | 148.44 | 233.3125 | 0.665579 |
| | ZK401^ | 177.36 | 166.03 | – | – |
| | D2815^ | 145.65 | 139.81 | – | – |
| QSGZ | D2804 | 162.83 | 154.08 | 249.7009 | 0.692617 |
| | D2807 | 153.31 | 146.20 | – | – |
| | D2811 | 156.01 | 148.44 | – | – |
| | YYT-1* | 185.96 | 173.03 | – | – |
| | YYT-2* | 185.26 | 172.46 | – | – |
| | YYT-3* | 188.37 | 174.99 | – | – |
| | YYT-4* | 183.79 | 171.27 | – | – |
| | Q502^ | 159.77 | 151.56 | – | – |
| | Q572^ | 125.10 | 122.49 | 239.8708 | 0.827619 |

Quartz[a]: no steam loss, $T = \frac{1309}{5.19 - lgC_{SiO2}} - 273.15$ (Fournier and Potter 1982); Quartz[b]: maximum steam loss,

$T = \frac{1522}{5.75 - lgC_{SiO2}} - 273.15$ (Fournier 1977). "^" means the data obtained from The Geothermal Geological Team of Tibet (1990);
"*" means the data obtained from Yuan et al. (2014); "–" represent no results
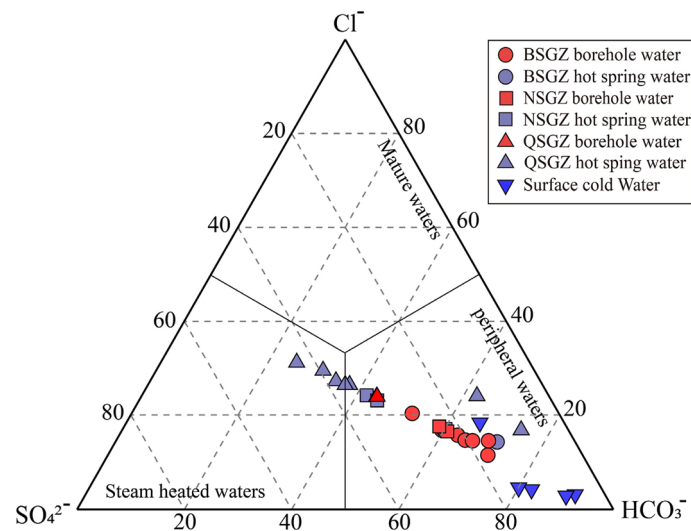


**Fig. 8** Cl–SO$_4$–HCO$_3$ ternary diagram for the water samples in YHGF

### Mixing evaluation of deep geothermal fluid with cold groundwater

The $Cl$–$SO_4$–$HCO_3$ triangular diagram has usually been used for the classification of water from non-thermal and thermal sources (Giggenbach 1991). All the surface waters and most of the hot springs and borehole waters plot in the peripheral region while the rest plot in the steam-heated region (Fig. 8), indicating mixing between the deep thermal water and cold groundwater, and the $SO_4^{2-}$ concentration in the high-temperature geothermal waters.

The conservative element Cl is hardly affected by water–rock interactions and is frequently used to study the hydrogeochemical processes by the relationship with major ions (Dotsika et al. 2006). The geothermal waters with higher concentrations of Cl (82–185 mg/L) have similar Na/Cl ratios (3–4) to surface river water with lower concentrations of Cl (1.8–6.9 mg/L), indicating the mixing between the geothermal waters and surface river water (Li et al. 2017a, b). Furthermore, in the diagram of Cl vs. Na (Fig. 9a), the favorable linear relationships of Cl–Na are displayed with $R^2$ of 0.93, indicating mixing during the ascent. A similar mixing signal is also observed in the diagrams of $SO_4^{2-}$, TDS, and B vs. Cl (Figs. 9b, 8c, and 9d) with $\underline{R}^2$ of 0.90, 0.95, and 0.91, respectively. Moreover, being different from Na, $SO_4^{2-}$, B, and TDS, the poor relation of Ca–Cl and Mg–Cl is shown (Fig. 9e, f). The Ca and Mg concentrations in the geothermal system were mainly controlled by the dissolution of carbonates or mixing with cold groundwater. As a result of the lack of Mg-rich and Ca-rich strata in the YHGF, we preclude the possibility of the dissolution of carbonates. Therefore, the deep geothermal waters were mixed with the cold groundwaters during ascent, forming the shallow lower temperature geothermal reservoir.
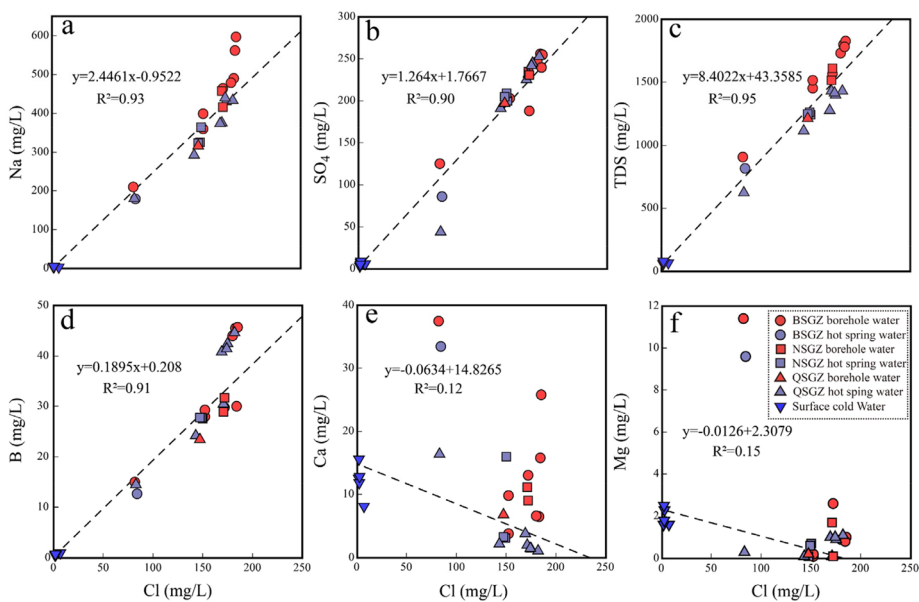


**Fig. 9** Diagram of Na vs. Cl, $SO_4$ vs. Cl, vs. Cl, B vs. Cl, Ca vs. Cl and Mg vs. Cl for the water samples in YHGF

*Silica–enthalpy mixing model*

In the mixing process of deep geothermal fluid with shallow cold groundwater, the $SiO_2$ concentration in thermal water is also reduced and usually results in lower reservoir temperature calculated by quartz (maximum steam loss) geothermometer. Therefore, to estimate the reservoir temperature more accurately, the silica–enthalpy mixing model was applied in the calculation of reservoir temperature in YHGF.

As deep thermal water rises to the surface, the enthalpy value and $SiO_2$ concentration of the deep thermal water will decrease to those of the mixed thermal water due to the mixing process of deep geothermal fluid with shallow cold groundwater (Fournier and Truesdell 1974). When the $SiO_2$ concentration and temperature of thermal water are in the equilibrium state, the enthalpy and $SiO_2$ concentration of deep thermal water show a functional relationship with those of mixed thermal water (Tong 1981). Based on the equilibrium between $SiO_2$ concentration and enthalpy, the silica–enthalpy mixing model was established by Fournier and Truesdell (1974). Therefore, the reservoir temperature and mixing proportion can be estimated by the silica–enthalpy mixing model, as shown in the following equation:

$$X1 = (S_h - S_s)/(S_h - S_c) \tag{5}$$

$$X2 = (SiO_{2h} - SiO_{2s})/(SiO_{2h} - SiO_{2c}) \tag{6}$$

where $S_h$ is the enthalpy of deep thermal water; $S_s$ is the enthalpy of mixed thermal water; $S_c$ is the enthalpy of surface cold water; $SiO_{2h}$ is the $SiO_2$ concentration of deep thermal water; $SiO_{2s}$ is the $SiO_2$ concentration of mixing thermal water; $SiO_{2c}$ is the $SiO_2$ concentration of surface cold water; $X1$ and $X2$ are the mixing proportion of shallow cold groundwater. To evaluate the mixing ratio, the graphical method proposed by Fournier and Truesdell (1974) was adopted. In the YHGF, because all the temperature of hot spring water is less than 100 ℃, the temperature of hot spring waters was adopted as the enthalpy values of mixed thermal water. The enthalpy values of surface cold water are 9 J/g. The mixing proportion of shallow cold groundwater and the reservoir temperature of the YHGF was estimated by Eqs. (5) and (6).

Since the $SiO_2$ concentration and temperature of some thermal waters are not in the equilibrium state, the temperature of the deep thermal waters has no intersection point with the mixing proportion of shallow cold groundwater (Wang Di, 2011). Therefore, some limitation conditions exist in the utilization of the silica–enthalpy mixing model. In YHGF, the silica–enthalpy mixing model was applied to calculate the reservoir temperature and mixing ratio of five water samples. The calculated results are listed in Table 3. The reservoir temperature of NSGZ range from 233.31 to 251.87 ℃, with a mixing proportion of shallow cold groundwater vary from 66.56% to 71.93%; the reservoir temperature of QSGZ range from 239.87 to 249.7 ℃, with a mixing proportion of shallow cold groundwater vary from 69.26% to 82.76% (Fig. 10).

## The calculation of the geothermal gradient and analysis of the heat transfer model

Obvious geothermal gradient differences exist in the various locations of the geothermal anomaly area (Xu and Guo 2009). In this study, based on the temperature logging
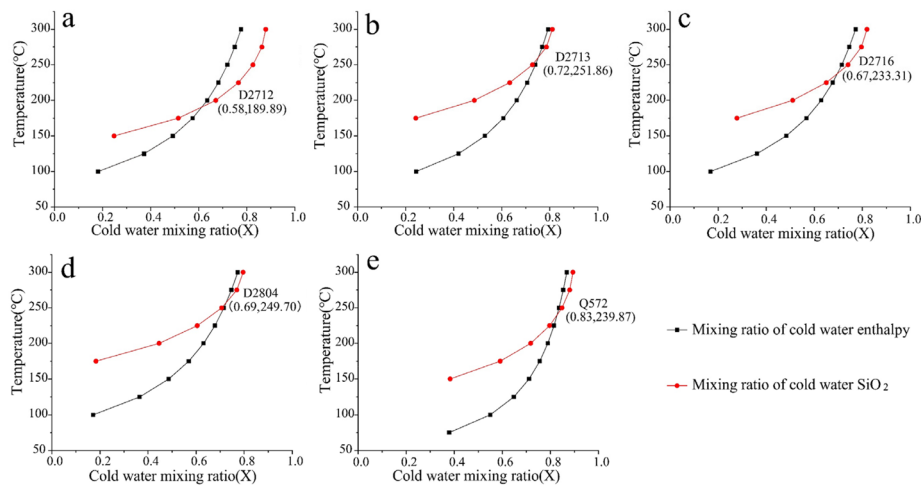
**Fig. 10** Relation between ratio of cold water and temperature in the mixing models from the thermal water samples

**Table 4** Geothermal gradient of borehole in YHGF

| borehole No | Depth(m) | G(℃/100 m) | G₀(℃/100 m) |
|---|---|---|---|
| ZK100 | 55 | 6.36 | 6.48 |
|  | 201 | 13.15 |  |
|  | 798 | 4.86 |  |
| ZK300 | 349 | 47.85 | 23.5 |
|  | 407 | 1.72 |  |
|  | 834 | 6.56 |  |
| ZK208 | 103 | 109.22 | 59.78 |
|  | 217 | 56.14 |  |
|  | 270 | 18.87 |  |
|  | 317 | 6.38 |  |

data from wells of the YHGF, the geothermal gradient of the YHGF was calculated using Eqs. (7) and (8). The result was calculated using the weighted average of the thickness of different segments of depth–temperature curve:

$$T(Z) = T_0 + GZ \tag{7}$$

$$T_0 = (T - G\sum Z)/n \tag{8}$$

where $T_0$ is the intercept between the straight line and the temperature coordinate axis; G is the geothermal gradient of different segments of depth–temperature curve; n is the number of measurement points. The result of the YHGF calculated by Eqs. (7) and (8) are listed in Table 4.

In YHGF, the borehole can be divided into two groups according to the characteristic of depth–temperature curve: (1) the conduction type borehole, which is not affected by groundwater activities, and its lithology is homogeneous formations. Furthermore, the
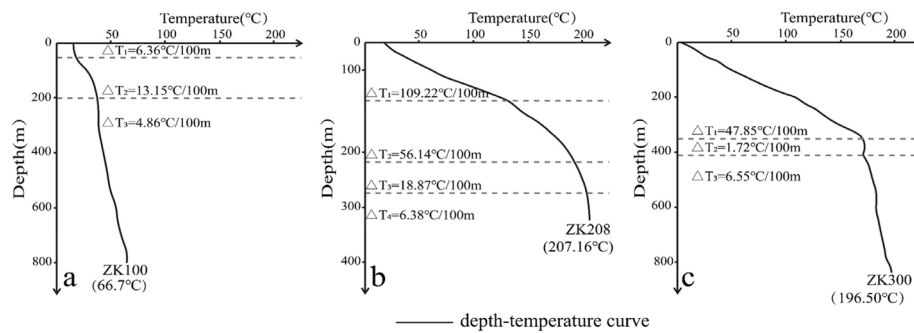
**Fig. 11** Depth–temperature curves of borehole in YHGF (modified from The Geothermal Geological Team of Tibet 1990)

temperature of the borehole shows a linear relationship with depth. (2) The conduction convection type borehole, which is affected by groundwater activities. Among them, the borehole is affected by infiltrating groundwater, its depth–temperature curve belongs to Concave-type when the equilibrium state of temperature with the surrounding rock is reached. The borehole is affected by upwelling thermal water, and its depth–temperature curve belongs to convex-type when equilibrium state of temperature with wall rock. The type of borehole is closely related to the geological structure and landform, as shown in Fig. 11.

### *Thermal conduction model*

Well ZK100 is located 1200 m to the south of BSGZ, which belongs to conduction type borehole without influence of groundwater activities, and its depth–temperature curve is close to a straight line. The geothermal gradient value of ZK100 is 6.48 ℃/100 m, which can be used as the regional geothermal gradient of YHGF. Therefore, according to the geothermal gradient, the terrestrial heat flow of YHGF can be determined using Eq. (9) proposed by Lang (2016):

$$q = -k(\mathrm{d}_T/\mathrm{d}_Z) \tag{9}$$

where $q$ is the terrestrial heat flow (mW m$^{-2}$); $k$ is rock thermal conductivity (W/m ℃); The negative sign indicates that the conduction direction of the heat flow; $(\mathrm{d}_T/\mathrm{d}_Z)$ is the geothermal gradient. According to the borehole data, the trachyandensite and volcanic breccia occurred from the surface to 350 m deep; 448 m thick granite occurred in the borehole range from 350 m to the bottom. The thermal conductivity of trachyandensite and volcanic breccia are 2.022 and 2.124 W/m ℃, respectively, with an average value of 2.073W/m ℃. The thermal conductivity of granite porphyry is 2.919W/m ℃. The geothermal gradient value of YHGF is 6.48 ℃/100 m. The terrestrial heat flow of YHGF calculated by Eq. (9) is 158.37 mW·m$^{-2}$. The terrestrial heat flow of YHGF is higher than those of the Tethys–Himalayan geothermal belt (30 to 80 mW m$^{-2}$) (Xu and Guo 2009; Xu et al. 2018), which indicates that the YHGF belongs to geothermal anomaly area.

### Combined conduction–convection heat transfer model

Some wells are affected by the upwelling thermal water, with a convex-type depth–temperature curve, and belong to a conduction–convection-type borehole. The ZK208, for instance, is located in the mountain pass of BSGZ. The geothermal gradient value of ZK208 is 59.78 ℃/100 m, which is about ten times the regional geothermal gradient. The reason may be that ZK208 is tectonically located in the junction of a near north–south fault ($F_3$) and near east–west fault ($F_{11}$), and the rock temperature is affected by the upwelling thermal water of high-temperature spring occurring around ZK208. The ZK300 is located in the gully between BSGZ and NSGZ. The geothermal gradient value of ZK300 is 23.50 ℃/100 m, which is about three times the regional geothermal gradient. Tectonically, ZK300 is located in the junction of $F_3$ and $F_{10}$. The upwelling thermal water led to an increase in the geothermal gradient and formed a montmorillonitization zone on the surface.

In general, the temperature of the earth is usually increased with depth, but the geothermal gradient can be affected by the decay of radioactive elements, geological structure, and groundwater. However, about 15 faults are distributed in YHTF, which play an important role in groundwater migration and lead to the change of temperature field. Compared with the conduction-type borehole, the geothermal gradient values of the conduction–convection-type borehole are relatively high and demonstrate the characteristic of vertical stratification. For example, the geothermal gradient of ZK300 is 47.85 ℃/100 m in the uppermost 0–349 m section and then decreases to 1.72 ℃/100 m between 349 and 407 m, to increase again to 6.56 ℃/100 m between 407 and 834 m. Due to the relatively small thermal conductivity difference of rock, this change in geothermal gradient is not caused by the change of thermal conductivity. Therefore, we suggest that the ZK300 and ZK208 are significantly affected by groundwater migration (upwelling thermal water). The depth–temperature curve of
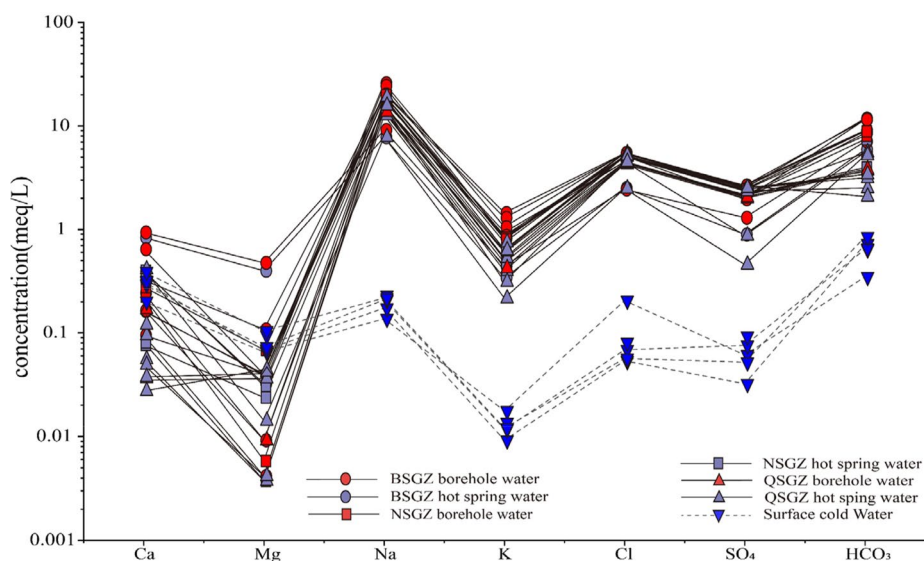


**Fig. 12** Schoeller diagram for the water samples in YHGF

ZK100 is close to a straight line, and its temperature is conducted from deep to the surface through a relatively homogeneous formation.

Furthermore, in YHTF, the geothermal gradient value and reservoir temperature show a decreasing trend from BSGZ to QSGZ, indicating that the heat source is located near BSGZ.

### Water–rock interaction in YHGF

In contrast to surface cold water, higher TDS values contributed by concentrations of major ions in the hot spring and borehole waters suggests a stronger water–rock interaction and dissolution of a large number of ions from the host rocks (Fig. 9c). As shown in the Piper diagram (Fig. 3), and semi-logarithmic Schoeller diagram (Fig. 12), the predominant ions in the surface cold water are $Ca^{2+}$, and $HCO_3^-$, while $Na^+$, $K^+$, $Cl^-$ and $HCO_3^-$ are the predominant ions in hot spring and borehole waters.

The high representation of geothermal waters fall in $Na–HCO_3$ and $Na–Cl$ facies in Fig. 3 indicates that water–rock interaction between the geothermal water and Na-silicate minerals might be responsible for the enrichment of $Na^+$, whereas the dissolution of silicate of carbonate minerals might be the source of $HCO_3^-$ in the water (Prasenjit et al. 2021). Similarly, $K^+$ may be originated in the dissolution of feldspars and micas during the water–rock interaction. Moreover, In the YHGF, granitic rocks such as biotite granite porphyry, porphyritic biotite granite, and trachyandesite are widely distributed in the deep, which could provide silicate minerals.

Most water samples have exhibited $\delta^{18}O$ drift in this study, particularly the hot water of QSGZ (Fig. 6b). There are two possible reasons for the "$\delta^{18}O$ drift" of geothermal water: (1) the evaporation effect of atmospheric precipitation. Since the evaporation of atmospheric precipitation results in the water enriched in heavy isotopes, the value of $\delta D$ increases less than those of $\delta^{18}O$. Therefore, the water sample points are inclined to the right of the meteoric line (Tian et al. 2014). (2) The isotope exchange effect during the water–rock interaction process. The rocks are richer in $^{18}O$ than the hot water. The isotopic exchange between the hot water and the rocks leads to an increase in the $\delta^{18}O$ value of the hot water (Martínez et al. 2021). As shown in Fig. 6a, the lighter "$\delta^{18}O$ drift" was observed in the water samples of atmospheric precipitation and surface cold water, suggesting the "$\delta^{18}O$ drift" is less affected by the evaporation effect in YHGF. Therefore, the isotope exchange effect during the water–rock interaction process is an important
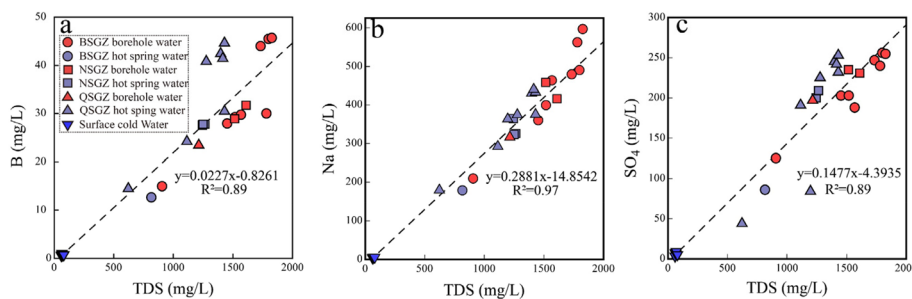


**Fig. 13** B, Na and $SO_4^{2-}$ concentrations plots as a positive correlation with TDS for water samples in YHGF

factor, which resulted in the $^{18}O$ enriched in the geothermal fluid of YHGF. The degree of "$\delta^{18}O$ drift" reflects that the water–rock interaction in QSGZ is stronger compared with those of BSGZ and NSGZ.

Due to the relatively stable nature of Sr and B isotopes in the boiling process of geothermal waters, Sr and B isotopes are widely used as a tracer for estimating the interaction between the host rocks and water (Graham 1992; Regensburg et al. 2016; Lu et al. 2018; Wen et al. 2018). Similar to TDS values, the B concentrations of geothermal water samples are distinctly higher than those of the cold water samples, and the content of TDS had a positive linear correlation with the B (Fig. 13a), suggesting the interaction between the geothermal waters and wall rocks interaction. According to the borehole, the Himalayan granitoid and pyroclastic rocks occur as wall rocks in the YHGF. The $\delta^{11}B$ values of geothermal waters are similar to the tourmalines that occur in Himalayan granitoid in the geothermal fields of Tibet, suggesting that the dissolution of tourmaline-rich granitic rocks is the primary factor controlling the boron concentrations (Aggarwal et al. 2003; Zhou et al. 2019; Fig. 4). Furthermore, strontium can readily move toward aqueous environment during water–rock interactions and the $^{87}Sr/^{86}Sr$ values of geothermal waters fall into the scope of wall rocks in YHGF, also indicate the water–rock interaction between the geothermal waters and Himalayan granitoid (Fig. 5). Therefore, the original geothermal waters have reacted with Himalayan granitoid along the flow path and the leaching of Sr/B from Sr/B-bearing minerals in the reservoir is the primary process affecting the Sr/B concentration (Yuan et al. 2014).

In general, the geochemistry of major ions (such as Na, K), trace elements (such as Sr, B), and O–H, Sr, and B isotopic characteristics in thermal waters was also studied for a better understanding of the hydrochemical processes in the geothermal system (Kaasalainen et al. 2015; Prasenjit et al. 2021). The above-mentioned O–H, Sr, and B isotopic characteristics indicate a stronger water–rock interaction between the geothermal water and host rocks. Furthermore, the average these ions concentration in geothermal waters, including hot springs and borehole waters, is higher than that in the surface cold water, indicating more contribution of solubility of these ions in the process of geothermal waters flow (Ramanathan and Chandrasekharam 1997; Singh et al. 2014).

### Conceptual model and the evolution of the geothermal fluid

Magnetotelluric survey and seismic prospecting reflected the partially molten granite as a low velocity–high conductive layer near the BSGZ northwest of the YHGF (The Geothermal Geological Team of Tibet 1990). Furthermore, reservoir temperatures calculated by the silica–enthalpy mixing model has been found that the geothermal fluid in BSGZ circulated rapidly and was discharged to the surface before reaching the chemical equilibrium. In addition, according to the current exploration of YHGF, the highest measured temperature and maximum flow capacity of deep geothermal fluid were exposed by the main production well ZK208 in BSGZ. Therefore, the major heat source of YHGF is magmatic, provided by a high-velocity conductive layer near the BSGZ located northwest of the YHGF.

According to the aggregation of conservative elements $Cl^-$ and $Li^+$ and the mixing region between meteoric and magmatic water in the plot of $\delta D$ vs. $\delta^{18}O$, these partially molten granites not only provided heat as a shallow magmatic heat source but also

contributed the chemical components to the deep geothermal fluid. Due to the topography of the YHGF and a large fracture system of cracks, faults, and pores, snow melt water infiltrated from the high-elevation mountain in the southwestern part and is heated up in the deep geothermal reservoir with the contributions of chemical components of the magmatic fluid.

The geothermal waters from YHGF have similar $^{87}Sr/^{86}Sr$ and $\delta^{11}B$ values and show a remarkable linear relationship of TDS vs. Cl, B, Na, and $SO_4^{2-}$ (Figs. 9c and 13), suggesting the deep and shallow reservoirs are within the same hydrothermal system. The flow tests of YHGF were performed by Wang (2018) and Shao et al. (2021). The results show that the tracer material of ZK202 was captured in ZK403 and ZK208, which indicates a direct hydraulic connection existed between BSGZ and north geothermal zones along the near north–south fault. Combining the exploration by geothermal wells, the positive oxygen shift of geothermal waters obtained with gradually decreased reservoir temperatures from the BSGZ to QSGZ, we suggested the deep geothermal waters were mixed with local cold groundwater and then flow northeastward, forming the shallow reservoir within the crushed zone and intersect spot of faults in the Himalayan granitoid. A similar phenomenon is observed in the Yangbajing geothermal field near YHGF in the same geothermal belt and suggests that the shallow reservoir of the Yangbajing geothermal field is formed due to the upward flow of the deep geothermal waters into the Quaternary loose sediments by mixing with cold groundwaters (Dor 2003; Guo et al. 2010). Furthermore, the original deep geothermal waters have reacted with wall rocks and more contribution of solubility of ions to shallow geothermal reservoirs in the process of geothermal water flow.

## Conclusions

Systematic fieldwork and geochemical analysis were carried out in the YHGF. The conclusions drawn from the study can be summarized as follows.

Based on the major element composition, the predominant ions in the surface cold water are $Ca^{2+}$ and $HCO_3^-$, while $Na^+$, $K^+$, $Cl^-$, and $HCO_3^-$ are the predominant ions in hot spring and borehole waters. The geothermal waters of the YHGF are mainly Na–$HCO_3$ facies, Na–$HCO_3$–Cl facies, and Na–Cl facies. From the trace elements and $\delta D$ and $\delta^{18}O$ values, geothermal waters of the YHGF are estimated to be of meteoric origin and affected by a magmatic fluid contribution. The recharge elevation of the geothermal water in YHGF range from 4850 and 6069.5 m, and there is a height difference of 100–900 m compared with the geothermal field, indicating the gravitational potential energy is an important driving force for ice–snow melt water to supply geothermal fields.

Due to the mixing process between the deep thermal water and cold groundwater, the relatively low reservoir temperature estimated by the quartz (maximum steam loss) geothermometer range from 153.21 to 227.72 ℃. Furthermore, the silica–enthalpy mixing model was used to calculate the reservoir temperature of NSGZ and QSGZ ranging from 233.31 to 251.87 ℃, with a mixing proportion of shallow cold groundwater varying from 66.56% to 82.76%. However, since the geothermal fluid in BSGZ circulated rapidly and was discharged to the surface before reaching the chemical equilibrium, the silica–enthalpy mixing model has not given results. Moreover, according to logging data, the geothermal gradient and terrestrial heat flow value of YHGF are 6.48 ℃/100 m and

Cao *et al. Geothermal Energy*      (2023) 11:23

Page 26 of 28

$158.37 \text{mW}\cdot\text{m}^{-2}$, respectively. The heat transfer models are mainly the thermal conduction model and the combined conduction–convection heat transfer model.

A stronger water–rock interaction existed between the geothermal water and host rocks. $Na^+$ and $HCO_3^-$ maybe originate in Na-silicate minerals and carbonate minerals, respectively. Similarly, $K^+$ may be originated in the dissolution of feldspars and micas in the granitoid. Most water samples have exhibited $\delta^{18}O$ drift in YHGF, particularly the hot water of QSGZ, which indicates that the water–rock interaction in QSGZ is stronger compared with those of BSGZ and NSGZ. Combining the hydrothermal tracer experiment, $^{87}Sr/^{86}Sr$ and $\delta^{11}B$ ratios obtained with gradually decreasing reservoir temperatures from the BSGZ to QSGZ, we suggested the major heat source is magmatic heat source near the BSGZ northwest of the YHGF, deep geothermal waters were mixed with cold groundwater and then flow northeastward, forming the shallow reservoir within the crushed zone and intersect spot of faults.

## Declarations

**References**
Aggarwal JK, Palmer MR, Bullen TD, Arnórsson S, Ragnarsdóttir KV. The boron isotope systematics of Icelandic geothermal waters: 1. Meteoric water charged systems. Geochim Cosmochim Acta. 2000;64:579–85.
Aggarwal JK, Sheppard D, Mezger K, Pernicka E. Precise and accurate determination of boron isotope ratios by multiple collector ICP-MS: origin of boron in the Ngawha geothermal system, New Zealand. Chem Geol. 2003;199(3–4):331–42.
Armijo R, Tapponnier P, Mercier JL, Han T-L. Quaternary extension in southern Tibet: Field observations and tectonic implications. J Geophys Res. 1986;91:13903.
Arnorsson S. Application of the silica geothermometer in low temperature hydrothermal areas in Iceland. Am J Sci. 1975;275(7):763.
Bob M, Rahman NA, Taher S, Elamin A. Multi-objective assessment of groundwater quality in Madinah City, Saudi Arabia. Water Qual Expo Health. 2015;7(1):53–66.
Cao R, Cao YB, Chen B, Bagas L, Yan SC, Huang C, Zhao H. Pegmatite magmatic evolution and rare metal mineralization of the Dahongliutan pegmatite field, Western Kunlun Orogen: constraints from the B isotopic composition and mineral-chemistry. Int Geol Rev. 2021;65(7):1224–42.
Coleman ML, Shepard TJ, Durham JJ, Rouse JE, Moore GR. Reduction of water with zinc for hydrogen isotope analysis. Anal Chem. 1982;54(6):993–5.
Coplen TB. Normalization of oxygen and hydrogen isotope data. Chem Geol. 1988;72(4):293–7.
Craig H. Isotopic variations in meteoric waters. Science. 1961;133:1702–3.
Dincer I, Acar C. A review on clean energy solutions for better sustainability. Int J Energy Res. 2015;39(5):585–606.

Cao *et al. Geothermal Energy*      (2023) 11:23

Page 27 of 28

Dor J. The basic characteristics of the Yangbajing geothermal field–a typical high temperature geothermal system. Eng Sci. 2003;5(1):42.

Dor J, Wang GL, Zheng KY. Study on the development and utilization strategy of geothermal resources in China. Beijing: Science Press; 2017.

Dotsika E, Leontiadis I, Poutoukis D, Cioni R, Raco B. Fluid geochemistry of the Chios geothermal area, Chios Island, Greece. J Volcanol Geoth Res. 2006;154(3–4):237–50.

Dotsika E, Poutoukis D, Kloppmann W, Guerrot C, Voutsa D, Kouimtzis TH. The use of O, H, B, Sr and S isotopes for tracing the origin of dissolved boron in groundwater in Central Macedonia. Greece Appl Geochem. 2010;25:1783–96.

Fournier RO. Chemical geothermometers and mixing models for geothermal systems. Geothermics. 1977;5:41–50.

Fournier RO, Potter RW. A revised and expanded silica (quartz) geothermometer. Geoth Res Counc Bull. 1982;11:3–9.

Fournier RO, Truesdell AH. Geochemistry applied to exploration for geothermal energy. Econ Geol 1974;69: 7.

Giggenbach WF. Geothermal solute equilibria Derivation of Na-K-Mg-Ca geoindicators. Geochim Cosmochim Acta. 1988;52(12):2749–65.

Giggenbach WF. Chemical techniques in geothermal exploration. Application of geochemistry in geothermal reservoir development 1991,119–144.

Giggenbach WF. Isotopic shifts in waters from geothermal and volcanic systems along convergent plate boundaries and their origin. Earth Planet Sci Lett. 1992;113:495–510.

Giggenbach WF, Gonfiantini R, Jangi BL, Truesdell AH. Isotopic and chemical composition of parbati valley geothermal discharges, Northwest Himalaya, India. Geothermics. 1983;12(2–3):199–222.

Graham IJ. Strontium isotope composition of Rotorua Geothermal waters. Geothermics. 1992;21:165–80.

Guo QH, Wang YX. Geochemistry of hot springs in the Tengchong hydrothermal areas, Southwestern China. J Volcanol Geotherm Res. 2012;215–216:61–73.

Guo QH, Wang YX, Liu W. Hydrogeochemistry and environmental impact of geothermal waters from Yangyi of Tibet, China. J Volcanol Geoth Res. 2009;180:9–20.

Guo QH, Wang YX, Liu WO. H, and Sr isotope evidence of mixing processes in two geothermal fluid reservoirs at Yangbajing, Tibet, China. Environ Earth Sci. 2010;59:1589–97.

Ha GH. Late Cenozoic normal faulting in the middle-southern segment of the East-Gulu Rift, South Tibet. Chinese Acad Geol Sci. 2019.

Hou ZQ, Gao YF, Qu XM, Rui ZY, Mo XX. Origin of adakitic intrusives generated during mid-Miocene east–west extension in southern Tibet. Earth Planet Sci Lett. 2004;220:139–55.

Jiang SY, Palmer MR. Boron isotope systematics of tourmaline from granites and pegmatites; a synthesis. Eur J Mineral. 1998;10:1253.

Jiang JS, Zheng YY, Gao SB, Zhang YC, Huang J, Liu J, Wu S, Xu J, Huang LL. The newly-discovered Late Cretaceous igneous rocks in the Nuocang district: products of ancient crust melting trigged by Neo-Tethyan slab rollback in the western Gangdese. Lithos. 2018;308:294–315.

Jin BF, Cheng LJ. Application of integrated geophysical method to geothermal exploration in Tibet// Selected papers of international Symposium on Exploitation and Utilization of high-temperature Geothermal in Tibet, China. 1992.

Kaasalainen H, Stefansson A, Giroud N, Arnorsson S. The geochemistry of trace elements in geothermal fluids, Iceland. Appl Geochem. 2015;62:207–23.

Karlsdottir MR, Heinonen J, Palsson H, Palsson O. High-temperature geothermal utilization in the context of european energy policy—implications and limitations. Energies. 2020;13:3187.

Lang XJ, Liu F, Liu ZM, Lin WJ, Xing LX, Wang GL. Terrestrial heat flow in guide basin, Qinghai. Geol Sci Technol Inf. 2016;35(3):227–32 (**in Chinese**).

Li J, Pang Z. The elevation gradient of stable isotopes in precipitation in the eastern margin of Tibetan Plateau. Earth Sci. 2022;65(10):1972–84.

Li J, Guo Q, Yu Z. Effect of clay mineral formation on accuracy of NA-K and K-Mg geochemical temperature scales in high-temperature geothermal system. Earth Sci. 2017a;42(01):142–54.

Li YM, Pang ZH, Yang FT, Yuan LJ, Tang PH. Hydrogeochemical characteristics and genesis of the high-temperature geothermal system in the Tashkorgan basin of the Pamir syntax, western China. J Asian J Sci. 2017b;149:134–44.

Lu L, Pang P, Kong Y, Guo Q, Wang Y, Xu C, Gu W, Zhou L, Yu D. Geochemical and isotope evidence on the recharge and circulation of geothermal water in the Tangshan Geothermal System near Nanjing, China: implications for sustainable development. Hydrogeol J. 2018;18:1–15.

Martínez-Florentino TAK, Esteller-Alberich MV, Expósito JL, Domínguez-Mariani E, Morales-Arredondo JI. Hydrogeochemistry and geothermometry of thermal springs in the eastern Trans-Mexican Volcanic Belt. Geothermics. 2021;96:1–18.

Mather JD, Porteous NC. The geochemistry of boron and its isotopes in groundwaters from marine and non-marine sandstone aquifers. Appl Geochem. 2001;16:821–34.

Michael K, Golab A, Shulakova V, Ennis-King J, Allinson G, Sharma S, Aiken T. Geological storage of $CO_2$ in saline aquifers–a review of the experience from existing storage operations. Int J Gas Control. 2010;5:659–67.

Musashi M, Nomura M, Okamoto M et al. Regional variation in the boron isotopic composition of hot-spring waters from Central Japan. Geochem. J. 1988;22:205–214.

Palmer MR. Boron isotope systematics of hydrothermal fluids and tourmalines: a synthesis. Chem Geol. 1991;94(2):111–21.

Palmer MR, Slack JF. Boron isotopic composition of tourmaline from massivesulphide deposits and tourmalinites. Contrib Mineral Petrol. 1989;103:434–51.

Palmer MR, Sturchio NC. The boron isotope systematics of the Yellowstone National Park (Wyoming) hydrothermal system: a reconnaissance. Geochim. Cosmochim. Acta 54, 1990;2811–2815.

Pang ZH. pH dependant isotope variations in arc-type geothermal waters: new insights into their origins. J Geochem Explor. 2006;89:306–8.

Pennisi M, Gonfiantini R, Grassi S, Squarci P. The utilization of boron and strontium isotopes for the assessment of boron contamination of the Cecina River alluvial aquifer (central-western Tuscany, Italy). Appl Geochem. 2006;21:643–55.

Prasenjit D, Maya K, Padmalal D. Hydrochemistry, geothermometry and origin of the low temperature thermal springs of South Konkan region. India Geothermics. 2021;90: 101997.

Qin JS. Hydrothermal Alteration and Evalution in Yangyi Geothermal Field. Journal of Taiyuan University of Technology. 2003;34(2):161–5.

Ramanathan A, Chandrasekharam D. Geochemistry of Rajapur and Puttur thermal springs of the West Coast, India. J Geol Soc. 1997;49:559–66.

Regensburg S, Feldbusch E, Norden B, Tichomirowa M. Fluid-rock interactions in a geothermal Rotliegend/Permo-Carboniferous reservoir (North German Basin). Appl Geochem. 2016;69:12–27.

Shao HB, Chen CF, Luo F, Chen XL, Wang SM. Review of yangyi phase I heat storage project. 2021 (Private report).

Shen Y, Zeng L, Gao J, Xu Q, Zhao L, Gao L, Hu Z, Wang Y. Oligocene-Miocene high Sr/Y magmatism and implications for deep processes of Qulin pluton in Gangdese batholith, southern Tibet. Acta Petrologica Sinica. 2020;36(9):2646–66.

Singh HK, Kumar Y, Chandrasekharam D, Gurav T, Singh B. High-heat-producing granites of East Dharwar Craton around Gugi, Karnataka, and their possible influence on the evolution of Rajapur thermal springs, Deccan Volcanic Province, India. Geotherm Energy. 2014;2(1):2.

Tan HB, Zhang YF, Zhang WJ, Kong N, Zhang Q, Huang JZ. Understanding the circulation of geothermal waters in the Tibetan Plateau using oxygen and hydrogen stable isotopes. Appl Geochem. 2014;51:23–32.

Tan, Q.Y. Study on the conceptual model of hydrothermal alteration [C]// Selected papers of the International Symposium on the Exploitation and Utilization of High Temperature Geothermal in Tibet, China. 1992.

Temizel EH, Fatma Gültekin, Ersoy AF et al. Multi-isotopic (O, H, C, S, Sr, B, Li) characterization of waters in a low-enthalpy geothermal system in Havza (Samsun), Turkey.Geothermics, 2021(97). https://doi.org/10.1016/j.geothermics.2021.102240.

The Geothermal Geological Team of Tibet. Exploration Report for the YangyiGeothermal Field of the Tibet Autonomous Region (in Chinese).1990.

Tian WG, Shao LY, Sun B, Zhao SP, Huo WG. Chemical behaviors of produced water from CBM wells in the Baode area Shanxi, China, and their control on gas accumulation. Nat Gas Ind. 2014;8:15–9.

Tong W, Liao Z, Liu S. Thermal springs in Tibet. Beiiing: Science Press; 1981. p. 170.

Trupti C, Minissale A, Vaselli O, Chandrasekharam D, Singh HK. Understanding the evolution of thermal fluids along the western continental margin of India using geochemical and boron isotope signatures. Geothermics. 2018;74:197–209.

Vengosh A, Starinsky A, Kolodny Y, Chivas AR. Boron isotope geochemistry as a tracer for the evolution of brines and associated hot springs from the Dead Sea, Israel. Geochim Cosmochim Acta. 1991;55:1689–95.

Vengosh A, Starinsky A, Kolodny Y, Chivas AR. Boron isotope geochemistry of thermal springs from the northern Rift Valley. Israel J Hydrol. 1994;162:155–69.

Wang Q, Zhu DC, Cawood PA, Zhao ZD, Liu SA, Chung SL, Zhang LL, Liu D, Zheng YC, Dai JG. Eocene magmatic processes and crustal thickening in southern Tibet: insights from strongly fractionated ca.43 Ma in the western Gangdese Batholtith. Lithos. 2015;329:128–41.

Wang S, Liu Z, Shao J. Hydrochemistry and H-O-C-S isotopic geochemistry characteristics of geothermal water in Nyemo-Nagqu. Tibet Acta Geologica Sinica. 2017;91(2):644–57.

Wang C, Li YJ, Wang HJ, Zhu SH, Chen J, Mei L, Liu XN. Tracer test on connectivity of mining and irrigation wells in Yangyi geothermal field, Tibet. Coal Geol China. 2018a;30(A01):5.

Wang DH, Zhang JF, Yang JJ, Jiang WL, Jiao QS. Application of remote sensing technology to the investigation of active faults in dangxiong area, Tibet. Geodesy Geody. 2018b;38(05):487–92 (**in Chinese**).

Wang CG, Zheng MP, Zhang XF, Xing EY, Zhang JY, Ren JH, Ling YO. H, and Sr isotope evidence for origin and mixing processes of the Gudui geothermal system, Himalayas, China. Geosci Front. 2020;11(4):1175–87.

Wang D. Formation mechanism of hot water and characteristics of geothermal field in gaoligong Mountain crossing section of Darui Railway. Chengdu University of Technology. 2011.

Wang SQ. Hydrogeochemical Processes and Genesis Mechanism of High-Temperature Geothermal System in Gudui, Tibet. D.S. Thesis. China University of Geosciences, Beijing (in Chinese with English abstract). 2017.

Wen T, Pinti DL, Castro MC, López-Hernández A, Hall CM, Shouakar-Stash O, Sandoval-Medina F. A noble gas and 87Sr/86Sr study in fluids of the Los Azufres geothermal field, Mexico – assessing impact of exploitation and constraining heat sources. Chem Geol. 2018;483:426–41.

Xu S, Guo Y. Fundamentals of geothermal science. Beijing: Science Press; 2009.

Xu P, Tan HB, Zhang YF, Zhang WJ. Geochemical characteristics and source mechanism of geothermal water in Tethys Himalaya belt. Geology in China. 2018;45(6):1142–54 ((**in Chinese with English abstract**)).

Yin A, Harrison TM. Geologic evolution of the Himalayan-Tibetan Orogen. Annu Rev Earth Planet Sci. 2000;28:211–80.

Yuan J, Guo Q, Wang Y. Geochemical behaviors of boron and its isotopes in aqueous environment of the Yangbajing and Yangyi geothermal fields, Tibet, China. J Geochem Explor. 2014;140:11–22.

Zhang J, Zhou L, Shao X, Zhang W, Feng Q. Investigation of the deep structures in Yang Yi geothermal field in Tibet Plateau by using converted waves of near earthquakes. Chin J Geophys. 1993;36(01):55–67.

Zhang WJ, Tan HB, Zhang YF, Wei HZ, Dong T. Boron geochemistry from some typical Tibetan hydrothermal systems: origin and isotopic fractionation. Appl Geochem. 2015;63:436–45.

Zheng YF, Chen JF. Stable isotope geochemistry. Beijing: Science Press; 2000. p. 148–50.

Zheng SH, Zhang ZF, Ni BL, Hou FG, Shen MZ. Hydrogen and oxygenstable isotope study of geothermal water in Tibet. Acta Sci Nauralium Univ Pekin. 1982;1:102–9 ((**in Chinese with English abstract**)).

Zhou Q, Li W, Wang G, Liu Z, Lai Y, Huang J, Yan G, Zhang Q. Chemical and boron isotopic composition of tourmaline from the Conadong leucogranite-pegmatite system in South Tibet. Lithos. 2019;326–327:529–39.

Zhu B, Zhu L, Shi C, Yu H. Geochemical exploration of geothermal fields. Geology Press; 1992, pp 84–91.

## Publisher's Note